Solving biharmonic equations with tri-cubic C^1 splines on unstructured hex meshes

Jeremy Youngquist and Jörg Peters
Department of Computer & Information Science & Engineering, University of Florida.

Abstract

Unstructured hex meshes are partitions of three-space into boxes that can include irregular edges, where $n \neq 4$ boxes meet along an edge, and irregular points, where the box arrangement is not consistent with a tensor-product grid. A new class of tri-cubic C^1 splines is evaluated as a tool for solving elliptic higher-order partial differential equations over unstructured hex meshes. Convergence rates for four levels of refinement are computed for an implementation of the isogeometric Galerkin approach applied to Poisson's and the biharmonic equation. The ratios of error are contrasted and superior to an implementation of Catmull-Clark solids. For the trivariate Poisson problem on irregularly partitioned domains the reduction by 2^4 in the L^2 norm is consistent with optimal convergence on a regular grid whereas the convergence rate for Catmull-Clark solids is measured as $O(h^3)$. The tri-cubic splines in the isogeometric framework correctly solve the trivariate biharmonic equation, but the convergence rate in the irregular case is lower than O(h^4). Optimal 2^4 reduction is achieved when the functions on the C^1 geometry are relaxed to be C^0.

Keywords: tri-cubic C^1 spline; unstructured hex-mesh; biharmonic equation; Catmull-Clark solids; irregular points and edges; Poisson's equation; convergence ratio

---

1. Introduction

Efficient representation of volumetric C^1 fields over hexahedral meshes is of interest in areas ranging from scientific data visualization to solving higher-order differential equations. For example, to visualize a flow computed by the Discontinuous Galerkin approach currently requires substantial post-processing to extract stream lines that the theory predicts to be smooth Walfisch et al. (2009). Engineering analysis based on splines is efficient in that it *a priori* bakes in the smoothness required of the solution of higher-order partial differential equations. Splines can serve both to define the geometry of the physical space and supply the degrees of freedom for numerical analysis on the manifold. The case of volumetric physical space, in three variables, is of obvious high practical interest. Where symmetries can not reduce dimension, splines need to be well-defined over unstructured partitions of the physical domain. In particular at irregularities, where the volumetric partition into boxes does not form a topological grid layout suitable for box-splines de Boor et al. (1993), the construction of smooth solutions is challenging. Unstructured partitions of the physical domain into boxes can include irregular edges, where $n \neq 4$ boxes meet along an edge, and irregular points, where $n \neq 8$ boxes meet. The challenge is that, at the irregularities, there is no consistent extension of the individual pieces' parametric derivatives to the whole neighborhood unless their cross-product vanishes (Peters and Reif, 2008, Lemma 3.7).

Until recently, the literature did not offer conforming polynomial C^1 splines over irregular box-complexes. One approach in two variables introduces a removable singularity into the parameterization at irregular points, see Peters (1991a); Reif (1998); Nguyen and Peters (2016); Toshniwal et al. (2017). This approach collapses the 1-jet of first derivatives at the irregularity and forces the 2-jet of second derivatives of the parameterization onto a linear map. Note that this approach differs structurally from the collapse of an edge as induced, for example, by the Duffy transform Duffy (1982). When used for surfaces embedded in 3-space, the main shortcoming of the collapse-project approach is poor surface shape near the singularity Karčiauskas and Peters (2017). However, for trivariate elements in 3-space shape aesthetics are not an issue. Wei et al. (2018) generalized the approach to three variables, but without smoothness near irregular edges, due to the 'challenging problem ... of how to impose C^1 continuity across spoke

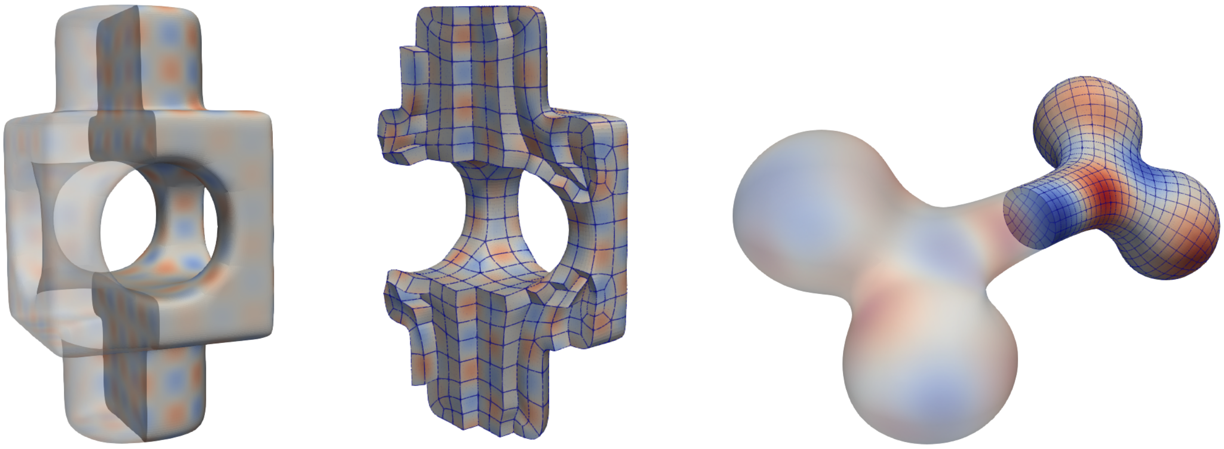

Figure 1: Using tri-3 C^1 splines to model smooth curved domains from box-complexes and solve volumetric higher-order partial differential equations on this geometry.

faces in an unstructured hex mesh'. Peters (2020) addressed the challenge and generalized the projection-collapse approach to three variables: the new spline space of tri-cubic (tri-3) splines with removable singularity is C^1 also across irregularities in unstructured hex meshes is nestedly-refinable and offers 2^3 degrees of freedom per box.

The goal is to measure the effectiveness of the new tri-3 C^1 splines for solving elliptic partial differential equations of order two and four. In particular, we want to track the convergence of numerical solutions where both the unstructured volumetric physical domain and the solution on the domain are represented as tri-3 C^1 splines, see Fig. 1. Using Galerkin's method, this generalizes the higher-order iso-parametric approach of Braibant and Fleury (1984); Shyy et al. (1988); Au and Cheung (1993); Schramm and Pilkey (1993) to unstructured volumetric physical domains, and is an instance of the isogeometric approach Cirak et al. (2000); Hughes et al. (2005).
Numerical experiments with four refinement steps, i.e. with up to half a million degrees of freedom, indicate

- 2^4 (fourth-order) convergence rate for Poisson equations also on irregular box-complexes,

i.e. the error between the computed and the known exact solution in the L^2 norm decreases by a factor of 2^4 under halving of the mesh interval h and by 2^3 in the H^1 error and 2^2 in the H^2 norm.
For the biharmonic (i.e. fourth-order, bi-Laplacian) equation, the observed convergence rate is also

- 2^4 for the regular case and for C^0 elements on C^1 geometry.

However, although still converging to the correct solution, the

- convergence rate of singular C^1 tri-3 splines on singular C^1 tri-3 spline geometry is less than 2^4 on irregular box-complexes.

We note that available a priori convergence estimates, e.g. of Bazilevs et al. (2006); Tagliabue et al. (2014), assume higher smoothness of the space, typically as high as for splines on the regular box-complex. That is, these estimates do not apply to solving the biharmonic equation with tri-3 C^1 splines. A likely explanation is that the singular, C^1-constrained tri-variate spline space does not have full approximation power. On the other hand, convergence is consistently better than that of Catmull-Clark solids MacCracken and Joy (1996); Burkhart et al. (2010):

- in all cases enumerated above, tri-3 C^1 splines exhibit faster convergence than Catmull-Clark solids.

Overview. After a brief literature review of trivariate smooth elements and the bivariate antecedents of tri-3 C^1 splines, Section 2 defines the tri-3 C^1 splines for unstructured box-complexes. The space is C^1 on local regular grids, C^2 if initialized by knot insertion on a locally tensor-product grid. The space has zero first derivatives across irregularities but is C^1 after a change of variables and has 2^3 linear independent B-spline-like basis functions per box. Section 4 shows the numerical convergence for Poisson's equation and compares the convergence to that of Catmull-Clark solids. Section 5 shows and discusses the convergence for the biharmonic equation and compares to Catmull-Clark solids.

2. Smooth trivariate finite elements

The grid points of a regular partition of 3-space into boxes can be interpreted as the control points of a trivariate tensor-product spline with one polynomial piece per cube. The theory of such splines is well-understood, see e.g. de Boor (1978, 1987). However complex outer shape and internal partition lead to unstructured hex-meshes, see Meyers and Tautges (1998); Mitchell (1999); Eppstein (1999); Yamakawa and Shimada (2002); Gregson et al. (2011); Johnen et al. (2017); Owen et al. (2017). Our improved understanding of fields via their singularity graph Nieser et al. (2011); Liu et al. (2018) has not been matched by corresponding progress to more flexible spline spaces. For box-complexes where the tensor-grid gives way to an irregular arrangement of boxes including irregular points and irregular edges, there are multiple options, none of them perfect.

Geometric continuity in three variables is in principle well-understood as a change of variables between pieces, see DeRose (1990); Peters (2002). In practice trivariate geometric continuity has been barely explored: Birner et al. (2018); Birner and Kapl (2019) join just one pair of trilinearly parameterized face-adjacent boxes and Kapl and Vitrih (2022) consider trilinearly parameterized multipatch volumes with exactly one inner (irregular) edge. The challenge is the complicated interaction of reparameterizations surrounding an irregular point. This complexity is particularly pronounced when the polynomial (tensor-)degree is low, below tri-5, which is important in three variables to obtain manageable spline spaces (tri-4 polynomial pieces already have 125 coefficients). Yet, geometric continuity requires increased polynomial degree near irregularities and careful book-keeping to adjust reparameterizations under refinement. – Generalized subdivision Catmull and Clark (1978); Doo and Sabin (1978); Peters and Reif (2008) creates an infinite sequence of nested piecewise polynomial layers that complicate analysis, e.g. computing integrals near irregularities. Trivariate subdivision rules analogous to Catmull-Clark subdivision Catmull and Clark (1978) have been proposed in MacCracken and Joy (1996) but come without guarantee of smoothness and approximation order. Burkhart et al. (2010) pioneered the use of Catmull-Clark solids in engineering applications. More recent work can be found in Altenhofen et al. (2021). Xie et al. (2020) solve the heat equation using interpolatory Catmull-Clark solids. We compare the convergence of the tri-3 C^1 splines to (non-interpolatory) Catmull-Clark solids.

Fixed-grid immersed representations, such as web-splines Höllig et al. (2001) or unstructured collections of radial basis functions Buhmann (2009) require careful adaptation of computations near the implicitly enforced boundaries. Penalty methods, Nitsche (1971) can add smoothness constraints as part of the solution process, at the cost of increasing the size of the problem. The approach requires a judicious choice of penalty parameters.

2.1. *Singular jet-collapse constructions in two variables*

There are three types of singular spline spaces in the bivariate case: (1) collapse of the domain as for generalized subdivision, (2) collapse of an edge or face as for polar constructions or Duffy-type Duffy (1982) elements with a removable singularity, or (3) collapse the set of derivatives (jets) at irregularities in the grid. This review focuses on the third option. Singular corner constructions that collapse the Taylor expansion (1-jet) at the irregular point by setting derivatives to zero have been proposed by Peters (1991a); Pfluger and Neamtu (1993); Neamtu and Pfluger (1994); Reif (1997, 1998); Bohl and Reif (1997); Nguyen and Peters (2016); Karčiauskas and Peters (2017); Toshniwal et al. (2017). The induced singularity side-steps the vertex enclosure problem Peters (1991b, 2002), a non-trivial algebraic requirement that arises from forcing the mixed parametric derivatives $\partial_u\partial_v f$ and $\partial_v\partial_u f$ to agree. Peters (1991a) suggested to simply set the mixed derivatives to zero and Reif (1997) proved that, if higher partial derivatives are suitably constrained, such singularities are locally removable. That is, the parametric singularity do not result in a loss of geometric smoothness. In contrast to subdivision, the singular corner approach yields a finite number of polynomial pieces compatible with existing CAD modeling environments. The resulting C^1 surfaces typically have poor shape when used for free-form design. A recent variant, proposed in Karčiauskas and Peters (2017), removes visible shape defects but at the cost of increased polynomial degree and overall complexity. After a gap of 20 years, Nguyen and Peters (2016) re-discovered the usefulness of singular parameterization to circumvent the challenges of refinement for engineering analysis and functions on irregular bivariate 2-manifolds. Combining the singular splines with PHT-splines Kang et al. (2015), (a.k.a. bi-cubic finite elements with hanging nodes in the finite element literature) yields a bi-cubic C^1 space with adaptive refinability. Nguyen and Peters (2016) demonstrate the space's effectiveness for modeling and solving thin plate challenge problems of the finite element obstacle course, such as the 'octant of a sphere' and the 'Scordelis-Lo roof'.

2.2. *Constructions in three variables*

Wei et al. (2018) base their spline space on tri-cubics but need no jet-collapse since the space is only C^0 across extraordinary edges and vertices. Their tri-cubic C012 splines have three types of degrees of freedom: C^2 spline control points (mesh vertices), C^1 spline control points (8 per box) and individual BB-coefficients near the irregularities (64 per box). Peters (2020) built a tri-3 C^1 spline space with singular parameterization. The space offers 8 degrees of freedom per box.

3. Tri-3 C^1 splines on unstructured box-complexes

This section gives a brief summary of the tri-3 C^1 splines defined in Peters (2020), starting with the definition of an unstructured box-complex. The spline space has 2^3 basis functions per box, see Fig. 2a. By default, the map $\mathbf{x} : R^3 \to \mathbb{R}^3$ that defines the geometry of the physical domain, is initialized by interpreting the vertices of the box-complex, wherever possible, as B-spline coefficients de Boor (1978, 1987). Knot insertion (averaging) converts the C^2 spline coefficients into C^1 spline coefficients (of a C^2 function). Then, at each irregularity, a well-behaved linear function is determined and composed with a singular local volumetric re-parameterization $\check{\mathbf{x}}$ consistent with the local layout of the box-complex. All first derivatives of $\check{\mathbf{x}}$ are continuous, albeit zero across irregularities. However, since the inverse $\check{\mathbf{x}}^{-1}$ is well defined, the local expansion of the linear function composed with $\check{\mathbf{x}}$ can be reparameterized to remove the singularity. The polynomial pieces of the spline space therefore join not just nominally C^1 (with a singularity), but smoothly over the whole box-complex. The tri-3 C^1 spline space can reproduce linear functions and is refinable. Each box with an irregularity is dyadically split into 2^3 sub-boxes to localize the operations that make the space C^1. Splitting allows irregular points to be in close proximity without interfering with one another, and simplifies the space's use for computations: every input box, regular or irregular, uniformly contributes exactly $2 \times 2 \times 2$ degrees of freedom.

Notation and Indexing Analogous to a simplicial complex, a *box-complex* (a.k.a. hex-mesh) in $\mathbb{R}^3$ is a collection of d-dimensional boxes, $0 \leq d \leq 3$, called d-boxes. Boxes of any dimension overlap only in complete lower-dimensional d-boxes. A 0-box is a vertex, a 1-box an edge, a 2-box a quadrilateral and a 3-box is a quadrilateral-faced hexahedron. A box without prefix is a 3-box.

Irregularities. For $d < 3$, an interior d-box is *regular* if it is completely surrounded by 2^{3-d} boxes and, for $3 > \bar{d} > d$, all incident $\bar{d}$-boxes are regular. For example, for a vertex to be regular, all edges incident to it must be regular. In R^3, a regular vertex ($d = 0$) is surrounded by 8 boxes, a regular edge ($d = 1$) by 4 boxes and a regular quadrilateral face ($d = 2$) by 2 boxes. Interior faces are always regular since they are shared by exactly 2^1 boxes.

Within stacked bi-variate irregularities, we define a 0-box to be *semi-regular box* (blue point in Fig. 2b) if (i) the box is shared by exactly two edges that are each surrounded by the same number of $n_e \neq 4$ boxes and (ii) the box is fully surrounded by $2n_e$ boxes. An edge connecting two semi-regular points is a *semi-regular edge*. A 1-box that is not a semi-regular edge but is surrounded by $n_e \neq 4$ boxes is called an *irregular edge*. A point that is neither regular nor semi-regular is an *irregular point*.

Boxes with at least one irregular point are evenly split into 2^m sub-boxes so that the sub-boxes contain at most one irregular point each. A box is regular if all its vertices are regular. Otherwise the box is irregular.

Example: Two layers of five boxes share a semi-regular point (blue in Fig. 2a). If the top and bottom 5-valent point are not semi-regular, the two edges forming the axis are irregular. If the stacked configuration were to continue to a third layer of five boxes, the middle edge is a semi-regular edge. The dotted lines in Fig. 2a hint at the partition of the C^1 spline into polynomial pieces near edge irregularities. Fig. 2b illustrates an irregular point enclosed by four boxes. ◇

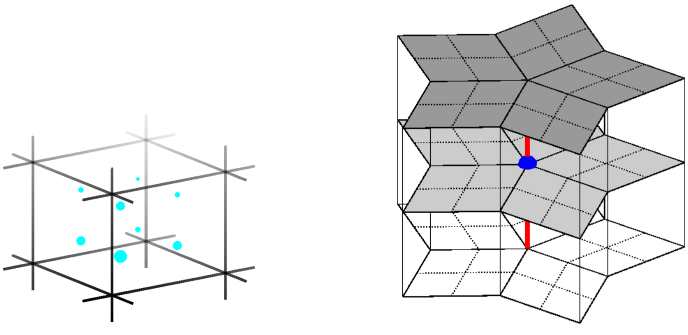

(a) (b) $3 = 3, d = 1$ (c) $3 = 3, d = 0, n = 4$

Figure 2: : (a) The 8 control abscissae $\mathbf{c}^s_\alpha$, (b,c) Irregularities. (b) Two irregular edges joining at a semi-regular vertex (●) due to stacking an irregular bivariate quadrilateral mesh.. (c) Four boxes in $\mathbb{R}^3$: one irregular point of valence $n = 4$ and four irregular edges of valence $n_1 = 3$.

Polynomial pieces, corner inner and index-wise nearest coefficients. A tri-3 C^1 spline consists of polynomial pieces $\mathbf{c}$ represented in tri-variate *tensor-product* Bernstein-Bézier (BB) form (see Farin (2002) or Prautzsch et al. (2002)):

$$\mathbf{c}(u,v,w) := \sum_{i=0}^{3}\sum_{j=0}^{3}\sum_{k=0}^{3} \mathbf{c}_{ijk} B_i^3(u) B_j^3(v) B_k^3(w). \quad \mathbf{u} := (u,v,w) \in \square := [0..1]^3, \quad \alpha := (i,j,k), \tag{1}$$

where $B_k^3(t) := \binom{3}{k}(1-t)^{3-k}t^k$ are the Bernstein-Bézier (BB) polynomials of degree 3 and the row vectors $\mathbf{c}_\alpha \in \mathbb{R}^m$ are the BB-coefficients. *De Casteljau's algorithm* can be used to evaluate the BB-form of Equation (1) and to re-express a polynomial on a subdomain of $[0..1]^3$. Connecting $\mathbf{c}_\alpha$ to $\mathbf{c}_{\alpha+e_j}$ whenever $\mathbf{c}_{\alpha+e_j}$ is well-defined, yields a mesh called the *BB-net*. Setting $\alpha_i := 0$ (or, symmetrically $\alpha_i := 3$) for exactly one $i \in \{1,2,3\}$ leaves 4×4 BB-coefficients that define $\mathbf{c}$ restricted to a quad face of the domain cube. Setting $\alpha_i := \alpha_j := 0$ for $i \neq j$ yields the BB-coefficients of a polynomial restricted to an edge E_k in the direction e_k, $i \neq k \neq j$. The 2^3 BB-coefficients $\mathbf{c}_\alpha$ with $\alpha \in \{0,3\}^3$ are called *corner BB-coefficients* since they are the values of $\mathbf{c}$ in the domain corners $\mathbf{u} \in \{0,1\}^3$. Two BB-coefficients $\mathbf{c}^s_\alpha$ and $\mathbf{c}^s_\beta$ are *index-wise nearest* if there is no $\mathbf{c}^s_\gamma$ with $\|\alpha - \gamma\|_1 < \|\alpha - \beta\|_1$ in the ℓ_1-norm.

The tri-3 C^1 splines. The splines are constructed by the following Algorithm 1.

Algorithm 1 Construction of tri-3 C^1 splines

Input: box-complex with vertices $\mathbf{v}_\beta$ and values v_β.
Output: Tri-3 C^1 splines

- Initialize the 2^3 inner BB-coefficients $\mathbb{b}^s_\alpha := (\mathbf{x}^s_\alpha, y^s_\alpha) \in \mathbb{R}^{3+1}$, $1 \leq \alpha_i \leq 2$ of each tri-3 piece by B-spline to BB-form conversion (knot insertion). In regular regions the splines are therefore initially C^2.
- Set the inner BB-coefficients of faces, the edges and finally the vertex as the average of their index-wise nearest neighbors.
- For irregular boxes only, apply de Casteljau's algorithm to split each tri-3 piece into 2^3 pieces.
- For irregular sub-boxes apply the operator $\mathbf{P}$ of the Appendix (from (Peters, 2020, Sect. 6)).

The isogeometric approach. Let $\square$ be a cube and

$$\mathbf{x} : \mathbf{s} \in \square \subset \mathbb{R}^m \to \xi = (\xi_1, \ldots, \xi_n) \in \Omega \subset \mathbb{R}^n$$

be the geometry map that defines the physical domain, see Fig. 3. The function $u : \square \subset \mathbb{R}^m \to \mathbb{R}$ is to be determined so that $u \circ \mathbf{x}^{-1}$ satisfies constraints, for example as a solution of the Poisson equation or the biharmonic equation.

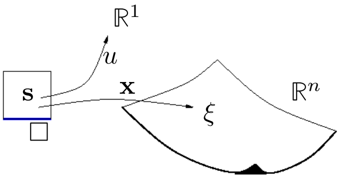

Figure 3: Isogeometric maps

4. Solving Poisson's equation over unstructured hex meshes

Wei et al. (2018) use a supercomputer implementation to solve Poisson's equation to analyze mechanical models similar to those Fig. 1. Their tri-variate splines are akin to Nguyen and Peters (2016) and therefore to the tri-3 C^1 splines in Peters (2020), but differ both in that they are truncated to transition from irregular to regular regions of C^2 tri-3 splines and require no jet-collapse because they are C^0 near irregular edges. For the Poisson equation, their numerical tests yield straight lines with a slope consistent with optimal convergence, e.g. $O(h^4)$ for the L^2 error. (They also point out that purely C^0 splines have too many degrees of freedom and that (finite) C^1 splines over irregular box-complexes, i.e. tri-3 C^1 splines, still await study in the literature.) For Catmull-Clark solids, combined with Wei et al. (2017), Wei et al. (2018) report sub-optimal convergence.

To ensure correct implementation of the tri-3 C^1 splines and the overall computational framework, and since the solution of second-order elliptic equations is of interest of its own right, we test the convergence of the tri-3 C^1 splines to the solution of Poisson's equation over the physical domain $\Omega = \mathbf{x}(\square)$:

$$\text{find } u : \Omega \to \mathbb{R} : \begin{cases} \Delta u &= -f \quad \text{in } \Omega, \\ \quad u &= 0 \qquad \text{on } \partial\Omega. \end{cases} \tag{2}$$

The weak form of Poisson's equation, projected into the C^1 space of basis functions B_j, i.e. Galerkin's approach, is

$$\int_\Omega \nabla u_h \cdot \nabla B_i(\mathbf{x}^{-1}) d_\Omega = \int_\Omega f B_i(\mathbf{x}^{-1}) d_\Omega, \qquad u_h := \sum_j \mathbf{c}_j B_j(\mathbf{x}^{-1}).$$

This can be rewritten as the matrix equation $K\mathbf{c} = \mathbf{f}$ to be solved for the coefficient vector $\mathbf{c}$ of u_h where

$$K_{ij} := \sum_\alpha \int_\square (\nabla B_i)^{\mathtt{t}} J_\alpha^{-\mathtt{t}} J_\alpha^{-1} (\nabla B_j) |\det J_\alpha| \, \mathrm{d}\square, \quad \mathbf{f}_i := \sum_\alpha \int_\square f \cdot \ B_i \cdot |\det J_\alpha| d\square. \tag{3}$$

Here the sum is over all pieces α where B_i has support and $J_\alpha := \nabla_{\mathbf{s}} \mathbf{x}_\alpha$. Boundary constraints are enforced following (Elman et al., 2014, Chapter 1): we split the set of basis functions $\{B_i\}$ into two sets: $\mathcal{I} := \{B_0, \cdots B_n\}$ and $\mathcal{B} := \{B_{n+1}, \cdots B_{n+n_\delta}\}$, with

$$u_h = \sum_{i=0}^{n} c_i B_i + \sum_{i=n+1}^{n+n_\delta} c_i B_i,$$

where the basis functions in $\mathcal{I}$ vanish on the boundary while those in $\mathcal{B}$ are nonzero on the boundary and vanish towards the interior. We set the coefficients of the functions in $\mathcal{B}$ to enforce the boundary conditions, leaving the basis functions in $\mathcal{I}$ free to solve the system of equations. For the convergence experiments, we chose $\Omega := [0, 6]^3$ partitioned as shown in Fig. 5, i.e. as a: tensor grid, 35-extruded mesh or sphere octant. To accurately measure the error, we chose

$$f := (6\pi^2/9) \sin((\pi x)/3) \sin((\pi y)/3) \sin((\pi z)/3). \tag{4}$$

Then the exact solution of (2) is

$$u = 2 \sin\left(\frac{\pi x}{3}\right) \sin\left(\frac{\pi y}{3}\right) \sin\left(\frac{\pi z}{3}\right). \tag{5}$$

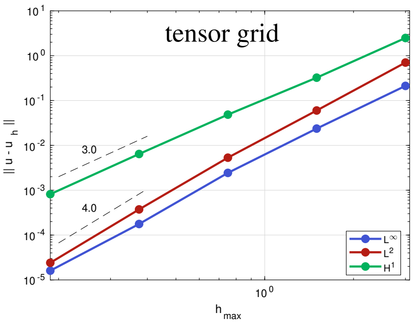

Figure 4: Optimal Poisson convergence

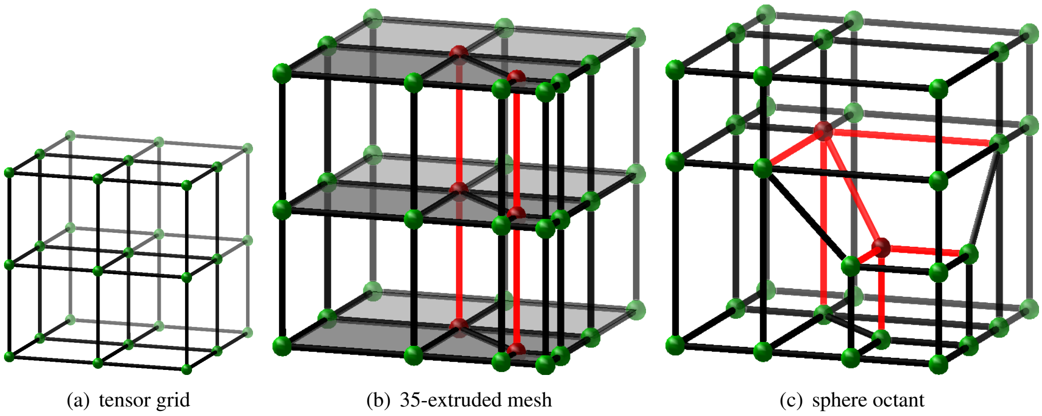
(a) tensor grid (b) 35-extruded mesh (c) sphere octant

Figure 5: Three main test box-complexes.

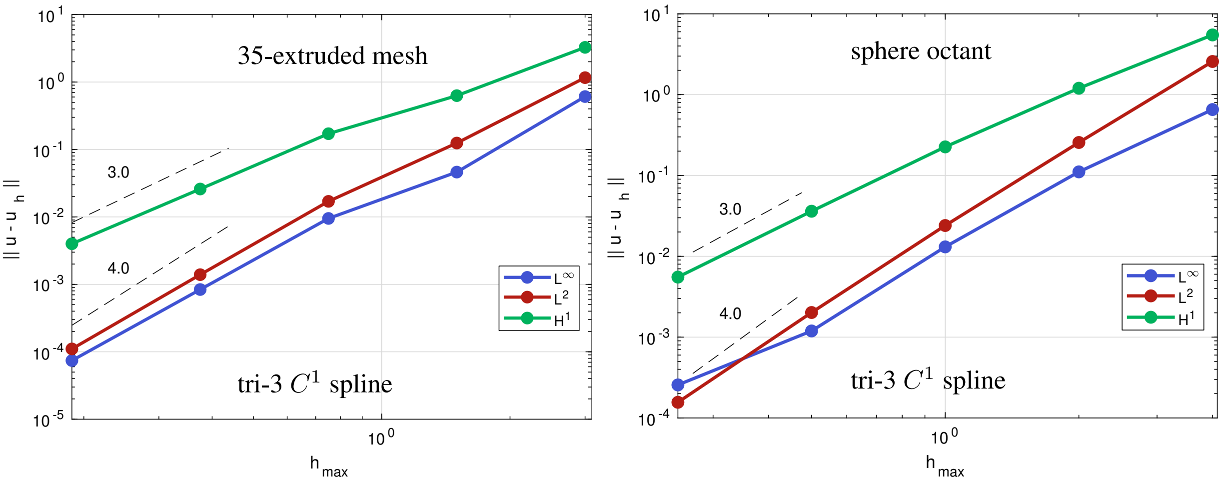

Figure 6: Poisson's equation solved in terms of the tri-3 C^1 spline. Error norms decreasing with h. The dashed lines labeled with n show slopes of 2^{-n}.

Starting with tensor grid as a basic 'sanity' test, we refine each of the three types of meshes, solve and measure the errors. The error plots in Fig. 4 and Fig. 6 are consistent with optimal $O(h^4)$.

The experiments ran on an Intel Core i7-6700K running at 4.0GHz with 16Gb of DDR4 RAM. The algorithm was implemented leveraging the data structures of OpenVolumeMesh Kremer et al. (2012), a C++ library. All integrals were computed using Gauss Quadrature with 4^3 Gauss points. The number of degrees of freedom in the test case tensor grid are 64, 512, 4,096, 32,768, and 262,144. This corresponds to, respectively, 8, 64, 512 4,096, and 32,768 hex elements, each with 8 degrees of freedom. The element count for 35-extruded mesh and sphere octant are very similar.

4.1. Comparison to Catmull-Clark solids

For further comparison and to calibrate with respect to a competing, easy-to-implement (in)finite element approach, we coded Catmull-Clark solids following MacCracken and Joy (1996); Burkhart et al. (2010). Catmull-Clark solids are assumed to be C^1 at irregular points C^1 across irregular edges, and C^2 elsewhere. In the bivariate setting Pan et al. (2016) report convergence of $O(h^2)$ and Liu et al. (2020) report an L^2 convergence of $O(h^{2.5})$ for the 35-mesh (one slice of the 35-extruded mesh). For trivariate interpolatory Catmull-Clark solids, (Xie et al., 2020, Fig 7) observe an initial decay in the L^2 error of $O(h^{3.52})$ with the error concentrated at irregularities. Catmull-Clark solids

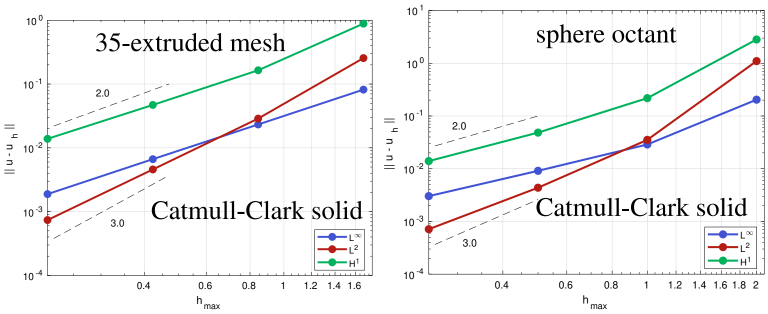

Figure 7: Volumetric Catmull-Clark elements: convergence of the error for Poisson's equation.

are therefore a natural competing representations for functions over unstructured box-complexes. Here the vertices of the input mesh are the degrees of freedom (as opposed to the 2^3 control points per box of the tri-3 C^1 spline). On sub-complexes without irregularities, the function can be evaluated using de Boor's algorithm. Otherwise, we locally perform Catmull-Clark solid subdivision until each Gauss point is enclosed by a regular neighborhood, so that we can evaluate. The coefficients of the outer boundary of the mesh are set to enforce (zero) Dirichlet boundary conditions. Fig. 7 shows the convergence of Catmull-Clark solids to the solution of the Poisson equation to be suboptimal and approximately $O(h^3)$.

5. Solving the biharmonic equation over unstructured hex meshes

One of the applications of the biharmonic equation is the stream function formulation of Stokes and Navier-Stokes equations. A classic approach, e.g. Ciarlet and Raviart (1974); Falk (1978); Arnold and Brezzi (1985), is to rewrite the biharmonic fourth-order partial differential equations as as a system of first order equations. Numerical solutions then typically require post-processing to yield a proper higher-order approximation. Using a finite difference multigrid approach, Pan et al. (2019) report solving on a tensor-product grid of size 512^3. Gómez et al. (2008) model fourth-order Cahn-Hilliard flow on a regularly partitioned cube. This and the T-spline constructions Wang et al. (2013, 2012) do not discuss convergence rates. For the regular tensor grid and C^2 splines Tagliabue et al. (2014) predicts a convergence of $O(h^4)$. Our implementation of tri-3 C^1 spline achieves this rate, also for a geometrically displaced grid, see Fig. 8.

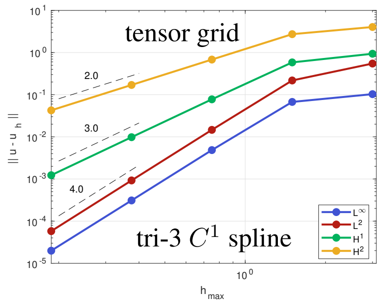

Figure 8: Optimal convergence, biharmonic on tensor grid.

To accommodate irregular box-complexes, discontinuous Galerkin elements with polygonal boundaries have been applied, see e.g. Wells et al. (2006); Xia et al. (2007); Mu et al. (2014). Koh et al. (2022) state optimal numerical convergence for quad meshes, but provide no data for hexahedral meshes. Their approach matches boundary data via a penalty function. Below, we will compare the results of tri-3 C^1 splines to Catmull-Clark solids on unstructured box-complexes. The authors of an efficient implementation of Catmull-Clark solids on unstructured box-complexes Altenhofen et al. (2021) were not aware of publications that cover Catmull-Clark solid convergence for fourth order equations. (Recall that the estimates of Bazilevs et al. (2006); Tagliabue et al. (2014) rely on higher than C^1 smoothness for fourth order problems and therefore do not apply.)

The biharmonic equation

$$\text{find } u : \Omega \to \mathbb{R} : \begin{cases} \Delta^2 u &= -f \quad \text{in } \Omega = \mathbf{x}(\Box), \\ \nabla u &= 0 \quad \text{on } \partial\Omega \\ u &= 0 \quad \text{on } \partial\Omega, \end{cases} \quad , \tag{6}$$

has the weak form

$$\int_\Omega \Delta u_h(\mathbf{x}^{-1}) \cdot \Delta B_i(\mathbf{x}^{-1}) d_\Omega = \int_\Omega f B_i(\mathbf{x}^{-1}) d_\Omega, \qquad u_h(\mathbf{x}^{-1}) := \sum_j \mathbf{c}_j B_j(\mathbf{x}^{-1}) \tag{7}$$

that can be rewritten as the matrix equation $K\mathbf{c} = \mathbf{f}$ to be solved for the vector of coefficients $\mathbf{c}$ where for $\xi = \mathbf{x}(\mathbf{s}) \in \Omega$,

$$K_{ij} := \sum_\alpha \int_\square (\Delta B_i(\mathbf{x}^{-1}(\xi)))(\Delta B_j(\mathbf{x}^{-1}(\xi)))|\det J_\alpha|\, \mathrm{d}\square, \quad \mathbf{f}_i := \sum_\alpha \int_\square f \cdot\, B_i \cdot |\det J_\alpha| d\square.$$

Here the sum is over all pieces α where B_i has support. By the chain rule, and denoting as $J^{-1}_{(:,k)}$ the kth column of the inverse of the Jacobian J of $\mathbf{x}$ and $\mathbf{s} := \mathbf{x}^{-1}(\xi)$,

$$\Delta_\xi(u_h \circ \mathbf{x}^{-1}) = \sum_{k=1}^{m} J^{-t}_{(:,k)} H J^{-1}_{(:,k)} + U \cdot X \qquad J(\xi) := (\nabla_\mathbf{s}\mathbf{x})(\mathbf{s}),\ H(\xi) := (\nabla_\mathbf{s}\nabla_\mathbf{s} u_h)(\mathbf{s}), \in \mathbb{R}^{m\times m},$$
$$X(\xi) := \Delta_\xi(\mathbf{x}^{-1}(\xi)),\ U(\xi) := (\nabla_\mathbf{s} u_h)(\mathbf{s}), \in \mathbb{R}^m. \tag{8}$$

For the convergence measurements, we chose $\Omega := [0,6]^3$ partitioned as shown in Fig. 5, and chose f so that the solution is

$$u = 8\sin^2\left(\frac{\pi x}{3}\right)\sin^2\left(\frac{\pi y}{3}\right)\sin^2\left(\frac{\pi z}{3}\right). \tag{9}$$

For Catmull-Clark solids we observe sub-optimal convergence in the first steps already on the perturbed tensor grid, see Fig. 9. On the 35-extruded mesh and sphere octant the convergence drops to sub-quadratic.

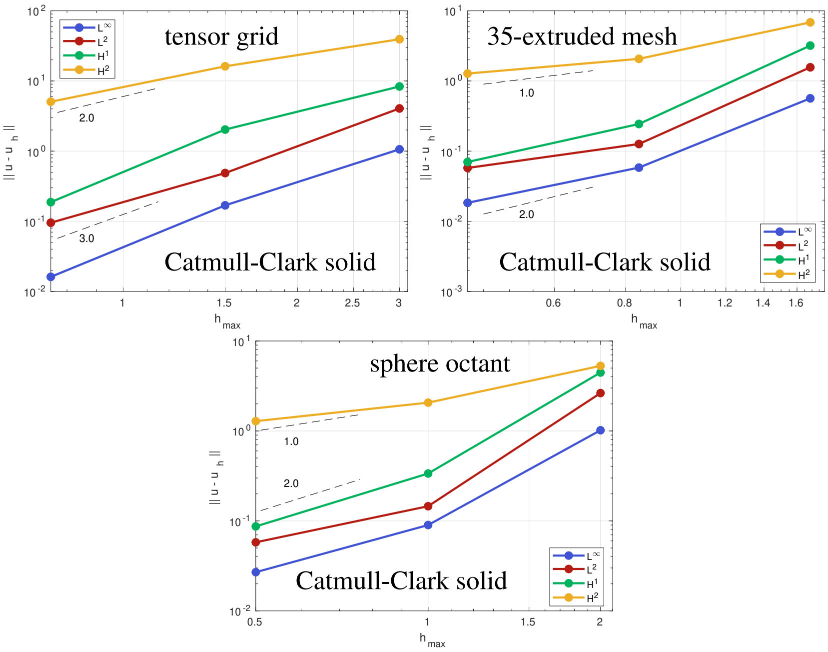

Figure 9: Volumetric Catmull-Clark convergence of the error for the biharmonic problem.

Fig. 10a indicates for tri-3 C^1 splines O(h^3) convergence in the L^2 norm and optimal convergence in the H^1 and H^2 norms for the 35-extruded mesh. For the sphere octant, see Fig. 10b, the convergence deteriorates notably in the third and fourth refinement. Since the computations do not betray any of the usual signs of a software bug and have been carefully and repeatedly checked – indeed the computations still converge – this observation points to

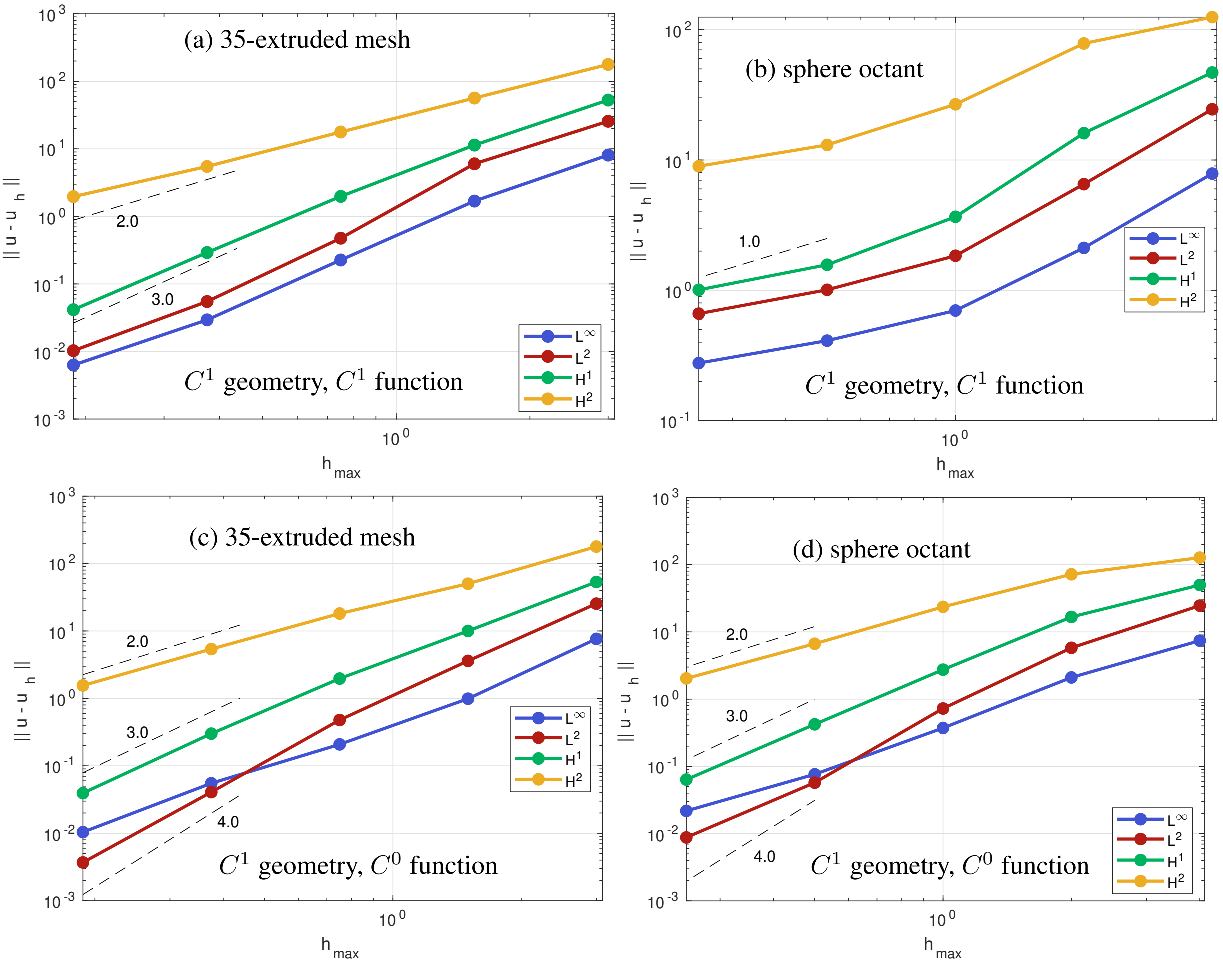
(a) 35-extruded mesh

(b) sphere octant

(c) 35-extruded mesh

(d) sphere octant

Figure 10: Convergence of tri-3 C^1 spline and variants for the biharmonic equation

a gap in the published theory of numerical convergence that, while intriguing, lies outside the scope of the present investigation into the numerical properties of tri-3 C^1 splines over box-complexes. As a further observation, the error on the tensor grid is maximal near high curvature. For the 35-extruded mesh and sphere octant the error is maximal near, but not at the irregularities. Finally, since the integrals in matrix K and right-hand side $\mathbf{f}$ are computed using Gauss points interior to each polynomial domain, K and $\mathbf{f}$ are well-defined, regardless of smoothness. However, when the space of functions permits jumps in the derivative that the weak formulation of the biharmonic equation does not allow, the solution of linear equation (7) may not be a solution to the Galerkin projection of the biharmonic equation. Nevertheless using the same C^1 parameterization $\mathbf{x}$ of the physical domain geometry, but relaxing the space of analysis functions u_h to be only C^0 – by not applying the projection $\mathbf{P}$ – yields near-optimal convergence rates also for the irregular meshes, see Fig. 10c,d.

6. Conclusion and future work

When solving the Poisson equation with tri-3 C^1 splines, the convergence rate is optimal, i.e. in line with the regular tensor-product case for the test problems. For biharmonic equations on unstructured hex meshes, the isogeometric approach using tri-3 C^1 spline converges to the correct solution. Intriguingly, the observed convergence rate in the irregular case is less than in the regular case – and an implementation error is very unlikely. Combining tri-3 C^1 spline geometry with C^0 functions in the isogeometric setting recovers the convergence rate of the regular tensor-product case. This indicates a knowledge gap in the theory of a priori numerical convergence estimates. A likely explanation is that the singular, tri-variate C^1 spline space lacks full approximation power at irregular points – and this raises the question whether and what cost-effective remedy exists and is needed to have maximal convergence rate for fourth order elliptic problems.

Acknowledgements. This work supported in part by DARPA TRADES and NIH EB018625.

References

Altenhofen, C., Ewald, T., Stork, A., Fellner, D., 2021. Analyzing and improving the parametrization quality of catmull-clark solids for isogeometric analysis. IEEE Computer Graphics and Applications 41. doi:10.1109/MCG.2021.3057905.

Arnold, D.N., Brezzi, F., 1985. Mixed and nonconforming finite element methods: implementation, postprocessing and error estimates. ESAIM: Mathematical Modelling and Numerical Analysis-Modélisation Mathématique et Analyse Numérique 19, 7–32.

Au, F., Cheung, Y., 1993. Isoparametric spline finite strip for plane structures. Computers & Structures 48, 22–32.

Bazilevs, Y., Beirao da Veiga, L., Cottrell, J.A., Hughes, T.J., Sangalli, G., 2006. Isogeometric analysis: approximation, stability and error estimates for h-refined meshes. Mathematical Models and Methods in Applied Sciences 16, 1031–1090.

Birner, K., Jüttler, B., Mantzaflaris, A., 2018. Bases and dimensions of C^1-smooth isogeometric splines on volumetric two-patch domains. Graphical Models 99, 46–56.

Birner, K., Kapl, M., 2019. The space of c1-smooth isogeometric spline functions on trilinearly parameterized volumetric two-patch domains. Computer Aided Geometric Design 70, 16–30.

Bohl, H., Reif, U., 1997. Degenerate Bézier patches with continuous curvature. Computer Aided Geometric Design 14, 749–761.

de Boor, C., 1978. A Practical Guide to Splines. Springer.

de Boor, C., 1987. B-form basics, in: Farin, G. (Ed.), Geometric Modeling: Algorithms and New Trends, SIAM. pp. 131–148.

de Boor, C., Höllig, K., Riemenschneider, S., 1993. Box Splines. Springer-Verlag, Berlin, Heidelberg.

Braibant, V., Fleury, C., 1984. Shape optimal design using B-splines. CMAME 44, 247–267.

Buhmann, M.D., 2009. Radial Basis Functions - Theory and Implementations. volume 12 of *Cambridge monographs on applied and computational mathematics*. Cambridge University Press.

Burkhart, D., Hamann, B., Umlauf, G., 2010. Iso-geometric finite element analysis based on Catmull-Clark subdivision solids. Comput. Graph. Forum 29, 1575–1584.

Catmull, E., Clark, J., 1978. Recursively generated B-spline surfaces on arbitrary topological meshes. Computer-Aided Design 10, 350–355.

Ciarlet, P.G., Raviart, P.A., 1974. A mixed finite element method for the biharmonic equation, in: Mathematical aspects of finite elements in partial differential equations. Elsevier, pp. 125–145.

Cirak, F., Ortiz, M., Schröder, P., 2000. Subdivision surfaces: a new paradigm for thin-shell finite-element analysis. International Journal for Numerical Methods in Engineering 47.

DeRose, T., 1990. Necessary and sufficient conditions for tangent plane continuity of Bézier surfaces. Computer Aided Geometric Design 7, 165–180.

Doo, D., Sabin, M., 1978. Behaviour of recursive division surfaces near extraordinary points. Computer-Aided Design 10, 356–360.

Duffy, M.G., 1982. Quadrature over a pyramid or cube of integrands with a singularity at a vertex. SIAM Journal on Numerical Analysis 19, 1260–1262.

Elman, H., Silvexter, D., Wathen, A., 2014. Finite Elements and Fast Iterative Solvers: with Applications in Incompressible Fluid Dynamics. Oxford Scholarship Online.

Eppstein, 1999. Linear complexity hexahedral mesh generation. CGTA: Computational Geometry: Theory and Applications 12.

Falk, R.S., 1978. Approximation of the biharmonic equation by a mixed finite element method. SIAM Journal on Numerical Analysis 15, 556–567.

Farin, G., 2002. Curves and Surfaces for Computer Aided Geometric Design: A Practical Guide. Academic Press, San Diego.

Gregson, J., Sheffer, A., Zhang, E., 2011. All-hex mesh generation via volumetric polycube deformation. Comput. Graph. Forum 30, 1407–1416.

Gómez, H., Calo, V.M., Bazilevs, Y., Hughes, T.J., 2008. Isogeometric analysis of the Cahn–Hilliard phase-field model. Computer Methods in Applied Mechanics and Engineering 197, 4333–4352. URL: https://www.sciencedirect.com/science/article/pii/S0045782508001953, doi:https://doi.org/10.1016/j.cma.2008.05.003.

Höllig, K., Reif, U., Wipper, J., 2001. Weighted extended B-spline approximation of dirichlet problems. SIAM J. Numerical Analysis 39.

Hughes, T.J.R., Cottrell, J.A., Bazilevs, Y., 2005. Isogeometric analysis: CAD, finite elements, NURBS, exact geometry and mesh refinement. Computer Methods in Applied Mechanics and Engineering 194, 4135–4195.

Johnen, A., Weill, J.C., Remacle, J.F., 2017. Robust and efficient validation of the linear hexahedral element. Procedia Engineering, Elsevier, Itl. Meshing Roundtable , +1–13.

Kang, H., Xu, J., Chen, F., Deng, J., 2015. A new basis for PHT-splines. Graphical Models 82, 149–159.

Kapl, M., Vitrih, V., 2022. C1 isogeometric spline space for trilinearly parameterized multi-patch volumes. Computers & Mathematics with Applications 117, 53–68.

Karčiauskas, K., Peters, J., 2017. Improved shape for refinable surfaces with singularly parameterized irregularities. Computer Aided Design 90, 191–198.

Koh, K.J., Toshniwal, D., Cirak, F., 2022. An optimally convergent smooth blended B-spline construction for semi-structured quadrilateral and hexahedral meshes. Computer Methods in Applied Mechanics and Engineering 399, 115438.

Kremer, M., Bommes, D., Kobbelt, L., 2012. OpenVolumeMesh - A Versatile Index-Based Data Structure for 3D Polytopal Complexes, in: 21st International Meshing Roundtable, Springer, San Jose, United States. pp. 531–548. URL: https://hal.inria.fr/hal-00762280, doi:10.1007/978-3-642-33573-0_31.

Liu, H., Zhang, P., Chien, E., Solomon, J., Bommes, D., 2018. Singularity-constrained octahedral fields for hexahedral meshing. ACM Trans. Graph 37, 93:1–93:17. URL: http://doi.acm.org/10.1145/3197517.3201344.

Liu, Z., McBride, A.T., Saxena, P., Steinmann, P., 2020. Assessment of an isogeometric approach with Catmull–Clark subdivision surfaces using the Laplace–Beltrami problems. Computational Mechanics 66. URL: https://doi.org/10.1007/s00466-020-01877-3, doi:10.1007/s00466-020-01877-3.

MacCracken, R., Joy, K.I., 1996. Free-form deformations with lattices of arbitrary topology, in: Proceedings of the ACM Conference on Computer Graphics, ACM, New York. pp. 181–188.

Meyers, R.J., Tautges, T.J., 1998. The ”hex-tet” hex-dominant meshing algorithm as implemented in cubit, in: Freitag, L.A. (Ed.), Itl. Meshing Roundtable, pp. 151–158. URL: http://imr.sandia.gov/papers/imr7.html.

Mitchell, S.A., 1999. The all-hex geode-template for conforming a diced tetrahedral mesh to any diced hexahedral mesh. Eng. Comput. (Lond.) 15, 228–235.

Mu, L., Wang, J., Ye, X., 2014. Weak Galerkin finite element methods for the biharmonic equation on polytopal meshes. Numerical Methods for Partial Differential Equations 30, 1003–1029.

Neamtu, M., Pfluger, P.R., 1994. Degenerate polynomial patches of degree 4 and 5 used for geometrically smooth interpolation in 3. Computer Aided Geometric Design 11, 451–474.

Nguyen, T., Peters, J., 2016. Refinable C^1 spline elements for irregular quad layout. Computer Aided Geometric Design 43, 123–130.

Nieser, M., Reitebuch, U., Polthier, K., 2011. Section 2: CUBE COVER — parameterization of 3D volumes. Computer Graphics Forum 30, 1397–1406.

Nitsche, J., 1971. Über ein Variationsprinzip zur Lösung von Dirichlet-problemen bei Verwendung von Teilräumen, die keinen Randbedingungen unterworfen sind, in: Abhandlungen aus dem mathematischen Seminar der Universität Hamburg, Springer. pp. 9–15.

Owen, S.J., Brown, J.A., Ernst, C.D., Lim, H., Long, K.N., 2017. Hexahedral mesh generation for computational materials modeling. Procedia Engineering, Elsevier, Itl. Meshing Roundtable , +1–13.

Pan, K., He, D., Ni, R., 2019. An efficient multigrid solver for 3d biharmonic equation with a discretization by 25-point difference scheme. arXiv: Numerical Analysis .

Pan, Q., Xu, G., Xu, G., Zhang, Y., 2016. Isogeometric analysis based on extended catmull–clark subdivision. Computers & Mathematics with Applications 71, 105–119. URL: `https://www.sciencedirect.com/science/article/pii/S089812211500543X`, doi:`https://doi.org/10.1016/j.camwa.2015.11.012`.

Peters, J., 1991a. Parametrizing singularly to enclose vertices by a smooth parametric surface, in: MacKay, S., Kidd, E.M. (Eds.), Graphics Interface '91, Calgary, Alberta, 3–7 June 1991: proceedings, Canadian Information Processing Society. pp. 1–7.

Peters, J., 1991b. Smooth interpolation of a mesh of curves. Constructive Approximation 7, 221–247.

Peters, J., 2002. Geometric continuity, in: Handbook of Computer Aided Geometric Design, Elsevier. pp. 193–229.

Peters, J., 2020. Refinable tri-variate C^1 splines for box-complexes including irregular points and irregular edges. Computer Aided Geometric Design 80, 1–21.

Peters, J., Reif, U., 2008. Subdivision Surfaces. volume 3 of *Geometry and Computing*. Springer-Verlag, New York.

Pfluger, P.R., Neamtu, M., 1993. On degenerate surface patches. Numerical Algorithms 5, 569–575.

Prautzsch, H., Boehm, W., Paluszny, M., 2002. Bézier and B-spline techniques. Springer Verlag.

Reif, U., 1997. A refinable space of smooth spline surfaces of arbitrary topological genus. Journal of Approximation Theory 90, 174–199.

Reif, U., 1998. TURBS—topologically unrestricted rational B-splines. Constructive Approximation 14, 57–77.

Schramm, U., Pilkey, W.D., 1993. The coupling of geometric descriptions and finite elements using NURBS - a study in shape optimization. Finite elements in Analysis and Design 340, 11–34.

Shyy, Y., Fleury, C., Izadpanah, K., 1988. Shape optimal design using higher-order elements. CMAME 71, 99–116.

Tagliabue, A., Dede', L., Quarteroni, A., 2014. Isogeometric analysis and error estimates for high order partial differential equations in fluid dynamics. Computers & Fluids 102, 277–303.

Toshniwal, D., Speleers, H., Hughes, T.J., 2017. Smooth cubic spline spaces on unstructured quadrilateral meshes with particular emphasis on extraordinary points: Geometric design and isogeometric analysis considerations. Computer Methods in Applied Mechanics and Engineering , 411–458.

Walfisch, D., Ryan, J.K., Kirby, R.M., Haimes, R., 2009. One-sided smoothness-increasing accuracy-conserving filtering for enhanced streamline integration through discontinuous fields. J. Sci. Comput 38, 164–184.

Wang, W., Zhang, Y., Liu, L., Hughes, T.J., 2013. Trivariate solid T-spline construction from boundary triangulations with arbitrary genus topology. Computer-Aided Design 45, 351–360.

Wang, W., Zhang, Y., Xu, G., Hughes, T.J., 2012. Converting an unstructured quadrilateral/hexahedral mesh to a rational T-spline. Computational Mechanics 50, 65–84.

Wei, X., Zhang, Y.J., Hughes, T.J.R., 2017. Truncated hierarchical tricubic spline construction on unstructured hexahedral meshes for isogeometric analysis applications. Computers & Mathematics with Applications 74, 2203–2220.

Wei, X., Zhang, Y.J., Toshniwal, D., Speleers, H., Li, X., Manni, C., Evans, J.A., Hughes, T.J., 2018. Blended B-spline construction on unstructured quadrilateral and hexahedral meshes with optimal convergence rates in isogeometric analysis. Computer Methods in Applied Mechanics and Engineering 341, 609 – 639.

Wells, G.N., Kuhl, E., Garikipati, K., 2006. A discontinuous Galerkin method for the Cahn–Hilliard equation. Journal of Computational Physics 218, 860–877.

Xia, Y., Xu, Y., Shu, C.W., 2007. Local discontinuous Galerkin methods for the Cahn–Hilliard type equations. Journal of Computational Physics 227, 472–491.

Xie, J., Xu, J., Dong, Z., Xu, G., Deng, C., Mourrain, B., Zhang, Y.J., 2020. Interpolatory Catmull-Clark volumetric subdivision over unstructured hexahedral meshes for modeling and simulation applications. Computer Aided Geometric Design 80, 101867. URL: `https://www.sciencedirect.com/science/article/pii/S0167839620300546`, doi:`https://doi.org/10.1016/j.cagd.2020.101867`.

Yamakawa, S., Shimada, K., 2002. Hexhoop: Modular templates for converting a hex-dominant mesh to an all-hex mesh. Eng. Comput. (Lond.) 18, 211–228.

Appendix: C^1 projector $\mathbf{P}$

This brief summary condenses the longer exposition and motivation of the steps in Peters (2020). We use the same notation. Applying $\mathbf{P}$ ensures C^1 continuity, via removable singularity, of the tri-3 C^1 splines corresponding to the irregular sub-boxes H^s, $s = 1, \dots, n$. Let $\mathbf{c}^s_\alpha \in \mathbb{R}^3$ be coefficients of H^s with $\mathbf{c}^s_\mathbf{0}$ the central irregular point. Denote by $\alpha \in T$ the labels of the direct neighbors of $\mathbf{c}^s_\mathbf{0}$ and by $\alpha \in G$ the labels of the 2-neighborhood of $\mathbf{c}^s_\mathbf{0}$. The values y_α for $\alpha \in T$ are collected in the n-vector y_T.

1. Compute a best-fit linear map ℓ to the BB-coefficients $\mathbf{c}^s_\alpha$, $\alpha \in T$, e.g. by computing a vector $\boldsymbol{\ell}$ as

$$\boldsymbol{\ell} := (b^{\mathtt{t}}_T b_T)^{-1} b^{\mathtt{t}}_T y_T \in \mathbb{R}^{3+1}, \quad b^t_T := (\dots, b^s_\alpha, \dots) \in \mathbb{R}^{3\times n}, \text{ (barycentric coordinates of the } \mathbf{c}^s_\alpha) \tag{10}$$
$$b^s_\alpha := \sigma[\mathbf{c}^s_\alpha, 1]M^{-1} \in \mathbb{R}^{3+1}, \alpha \in T, \quad \sigma := \sum_{s=1}^{n}\sum_{j=1}^{3} \frac{\|\mathbf{c}^s_\mathbf{0} - \mathbf{c}^s_{e_j}\|}{3n}, \quad M^{-1} := \begin{bmatrix} -1 & 1 & 1 & -1 \\ 1 & -1 & 1 & -1 \\ 1 & 1 & -1 & -1 \\ 1 & 1 & 1 & 1 \end{bmatrix} /4.$$

2. For each irregular sub-box H^s, compute the polyhedral intersection $\mathbf{q}^s$ by solving the 9×9 system

$$[\mathbf{q}^s, \mu] \begin{bmatrix} I_3 & I_3 & I_3 \\ C_1 & \mathbf{0} & \mathbf{0} \\ \mathbf{0} & C_2 & \mathbf{0} \\ \mathbf{0} & \mathbf{0} & C_3 \end{bmatrix} = \left[\mathbf{c}^s_{2e_1}, \mathbf{c}^s_{2e_2}, \mathbf{c}^s_{2e_3}\right], \quad \mathbf{0} \in \mathbb{R}^{2\times 3}, \mu \in \mathbb{R}^6. \tag{11}$$

   where I_3 is the 3×3 identity matrix, $e_j(i) = 1$ for $i = j$ and zero otherwise are the (local unit) labels of the three directions emanating from the irregular corner of H^s, n_k is the valence of the edge with label e_k and $C_k \in \mathbb{R}^{2\times 3}$ are first two rows of $Q_{n_k}(\mathbf{c}_{2e_k+e_j} - \mathbf{c}_{2e_k})$, $j \neq k$ where Q_{n_k} is defined in (15). Check that the system is well-conditioned, i.e. the sub-box is well-formed (Peters, 2020, Def 2)).
3. For each irregular sub-box H^s, compute the BB-coefficients of the singular parameterization $\breve{\mathbf{x}}^s$ by

$$\breve{\mathbf{x}}^s_\alpha := \begin{cases} \breve{\mathbf{x}}^s_\mathbf{0} := \sum_{j=1}^{n} \mathbf{q}^j/n, & \text{if } \alpha_1, \alpha_2, \alpha_3 < 2; \quad \text{(singularity)} \\ \mathbf{c}^s_\alpha & \text{if } \alpha_k = 2, \alpha_i, \alpha_j \in \{0,1\};\ \text{and } n_k = 4; \\ \breve{\mathbf{x}}^s_{2e_k} := \sum_{j=1}^{n_k} \mathbf{q}^{jk}/n_k, & \text{if } \alpha_k = 2, \alpha_i, \alpha_j \in \{0,1\};\ \text{and } n_k \neq 4; \\ \mathbf{q}^s + \frac{2-\alpha_i}{4}(\mathbf{q}^{jk} - \mathbf{q}^s) & \text{if } \alpha_k = 2, \alpha_j = 2,\ \alpha_i \in \{0,1\} \text{ and } n_k \neq 4. \end{cases} \tag{12}$$

4. For each irregular sub-box H^s, for $\alpha \in G$,

$$\mathbf{x}^s_\alpha := \breve{\mathbf{x}}^s_\alpha, \qquad y^s_\alpha := \ell(\breve{\mathbf{x}}^s_\alpha) = \breve{b}^s_\alpha \boldsymbol{\ell} \in \mathbb{R}, \quad \text{where } \breve{b}^s_\alpha := [\breve{\mathbf{x}}^s_\alpha, 1]M^{-1}. \tag{13}$$

   For each inner BB-coefficient of a semi-regular edge of valence n the *bi-variate 2-neighborhood 'orthogonal' to the edge* is transformed via the jet-collapse and projection P_n. P_n is applied to each coordinate c^σ_α of $(\mathbf{c}^s_\alpha, y^s_\alpha)$ separately, generating $x_{ab} := (x^s_{ab})_{s=1,\dots,n} \in \mathbb{R}^n$ defined by

$$x^s_{11} := x^s_{10} := x^s_{01} := x^s_{00} := \frac{1}{3n}\sum_{\sigma=1}^{n} c^\sigma_{11} + c^\sigma_{21} + c^\sigma_{12} \in \mathbb{R}, \quad s = 1, \dots, n, \tag{14}$$

$$x_{21} := x_{00} + \kappa Q_n\Big(2(c_{21} + c_{\overleftarrow{12}}) + c_{\overrightarrow{21}} + c_{12}\Big) \in \mathbb{R}^n, \quad Q_n := \left(\cos\frac{2\pi(i-j)}{n}\right)_{i=1..n,j=1..n} \in \mathbb{R}^{n\times n},$$
$$x_{12} := x_{00} + \kappa Q_n\Big(c_{21} + c_{\overleftarrow{12}} + 2(c_{\overrightarrow{21}} + c_{12})\Big) \in \mathbb{R}^n, \quad \kappa_{\text{default}} := \frac{\sqrt{2}}{4n\cos\frac{\pi}{n}}. \tag{15}$$

5. For every face with BB-coefficients $\mathbf{c}_{ij0}$ shared by an irregular sub-box H^a and a (regular or irregular) sub-box H^b, enforce regular C^1 continuity by averaging

$$\mathbb{b}^a_{ij0} = \mathbb{b}^b_{ij0} := (\mathbb{b}^a_{ij1} + \mathbb{b}^b_{ij1})/2, \qquad \mathbb{b}^a_\alpha := (\mathbf{c}^s_\alpha, y^s_\alpha).$$